

# Selective Urea Electrosynthesis from CO<sub>2</sub> and Nitrate on Spin-Polarized Atomically Ordered PdCuCo

Mengqiu Xu, Hang Zhou, Ximeng Lv, Yuqiang Fang, Xueyang Tu, Fang Wang, Qing Han,\*  
Xuelu Wang,\* and Gengfeng Zheng\*

The electrocatalytic conversion of NO<sub>3</sub><sup>−</sup> and CO<sub>2</sub> into urea features a potential means of reducing carbon footprint and generating value-added chemicals. Nonetheless, due to the limited efficiency of carbon–nitrogen (C–N) coupling and the competing side reaction that forms ammonia, the urea selectivity and production yield have remained low. In this work, a spin–polarized cobalt–doped, atomically ordered PdCu intermetallic compound (denoted as PdCuCo) is developed as an efficient urea electrosynthesis catalyst. The Pd and Cu serve as the adsorption sites for CO<sub>2</sub> and NO<sub>3</sub><sup>−</sup>, respectively, and the spin–polarized Co sites promote the adsorption of \*NO intermediate, followed by hydrogenation of \*NO at its N–terminal to form \*HNO, instead of at its O–terminal. The difference in the hydrogenation position switches the subsequent reaction pathway to produce urea, in contrast to the PdCu or Ni–doped PdCu intermetallic compounds with main product selectivity of ammonia. The PdCuCo electrocatalyst exhibited an outstanding electrosynthesis of urea from NO<sub>3</sub><sup>−</sup> and CO<sub>2</sub>, including a Faradaic efficiency of 81%, a high urea yield of 227 mmol g<sub>cat.</sub><sup>−1</sup> h<sup>−1</sup>, and a notable electrochemical stability of >260 h, suggesting the attractive potential of designing spin–polarized catalytic sites for carbon–nitrogen coupling processes.

## 1. Introduction

Urea is a widely used chemical in agricultural and industrial production, with its global consumption over 188 million metric tons annually.<sup>[1]</sup> The urea synthesis method in industry relies predominantly on Bosch–Meiser process, which is high energy demanding and carbon–emission intensive.<sup>[2]</sup> The recent development of electrochemical urea synthesis using NO<sub>3</sub><sup>−</sup> and CO<sub>2</sub>, ideally powered by renewable energy,<sup>[3]</sup> features a potential and sustainable strategy for achieving value–added products and carbon neutrality.<sup>[4]</sup> The urea electrosynthesis involves a multi–step proton and electron transfer process and the pivotal C–N coupling, and entails rational design of efficient catalytic sites to expedite the slow charge transfer and reaction kinetics.<sup>[5]</sup>

A variety of electrocatalysts, mostly metal alloys and (hydro)oxides with adjacent bi–metallic sites, such as Zn/Cu,<sup>[5a]</sup> Pd/Cu–Ni(OH)<sub>2</sub>,<sup>[5b]</sup> CuWO<sub>4</sub>,<sup>[6]</sup> and Sb<sub>x</sub>Bi<sub>1−x</sub>O<sub>y</sub> clusters,<sup>[7]</sup> have been demonstrated to catalyze the co–electroreduction of NO<sub>3</sub><sup>−</sup> and CO<sub>2</sub> to urea. For instance, the Sargent group reported a Zn/Cu

bilayer can stabilize key intermediates via a relay catalytic mechanism to improve the urea selectivity.<sup>[5a]</sup> Ye and coworkers found that the atomically dispersed Cu in Pd lattice can reduce NO<sub>3</sub><sup>−</sup> to \*NH<sub>2</sub>, as well as lower the energy barrier of the C–N coupling between \*NH<sub>2</sub> and \*CO.<sup>[5b]</sup> On the other hand, during the urea electrosynthesis, the major competing reaction is the direct NO<sub>3</sub><sup>−</sup> reduction reaction (NO<sub>3</sub>RR) to ammonia (NH<sub>3</sub>) via fast catalytic hydrogenation of N (i.e., N–H coupling),<sup>[8]</sup> which is generally more predominant than the C–N coupling step to urea. To date, the capability of controlling the C–N coupling over the N–H or C–H coupling is still quite limited, even for the adjacent bimetallic sites. As a consequence, the electrochemical urea synthesis performances have remained suboptimal, with the Faradaic efficiencies of urea (FE<sub>urea</sub>) generally below 50% and the urea production rates <65 mmol•g<sub>cat.</sub><sup>−1</sup>•h<sup>−1</sup>.

Previous theoretical calculations have indicated that a key bifurcation point between the urea and ammonia formation pathways is the hydrogenation of the \*NO intermediate bound on the catalytic metal sites.<sup>[9]</sup> As shown in Figure 1a, the hydrogenation

M. Xu, X. Lv, Q. Han, G. Zheng  
Laboratory of Advanced Materials  
State Key Laboratory of Porous Materials for Separation and Conversion  
Shanghai Key Laboratory of Molecular Catalysis and Innovative Materials  
Fudan University  
Shanghai 200438, China  
E-mail: [qhan@fudan.edu.cn](mailto:qhan@fudan.edu.cn); [gfzheng@fudan.edu.cn](mailto:gfzheng@fudan.edu.cn)

H. Zhou, F. Wang, X. Wang  
Physics Department & Shanghai Key Laboratory of Magnetic Resonance  
School of Physics and Electronic Science  
East China Normal University  
Shanghai 200062, China  
E-mail: [xlwang@phy.ecnu.edu.cn](mailto:xlwang@phy.ecnu.edu.cn)

Y. Fang, X. Tu  
School of Materials Science and Engineering  
Shanghai Jiao Tong University  
Shanghai 200240, China

The ORCID identification number(s) for the author(s) of this article can be found under <https://doi.org/10.1002/adma.202505286>

DOI: 10.1002/adma.202505286

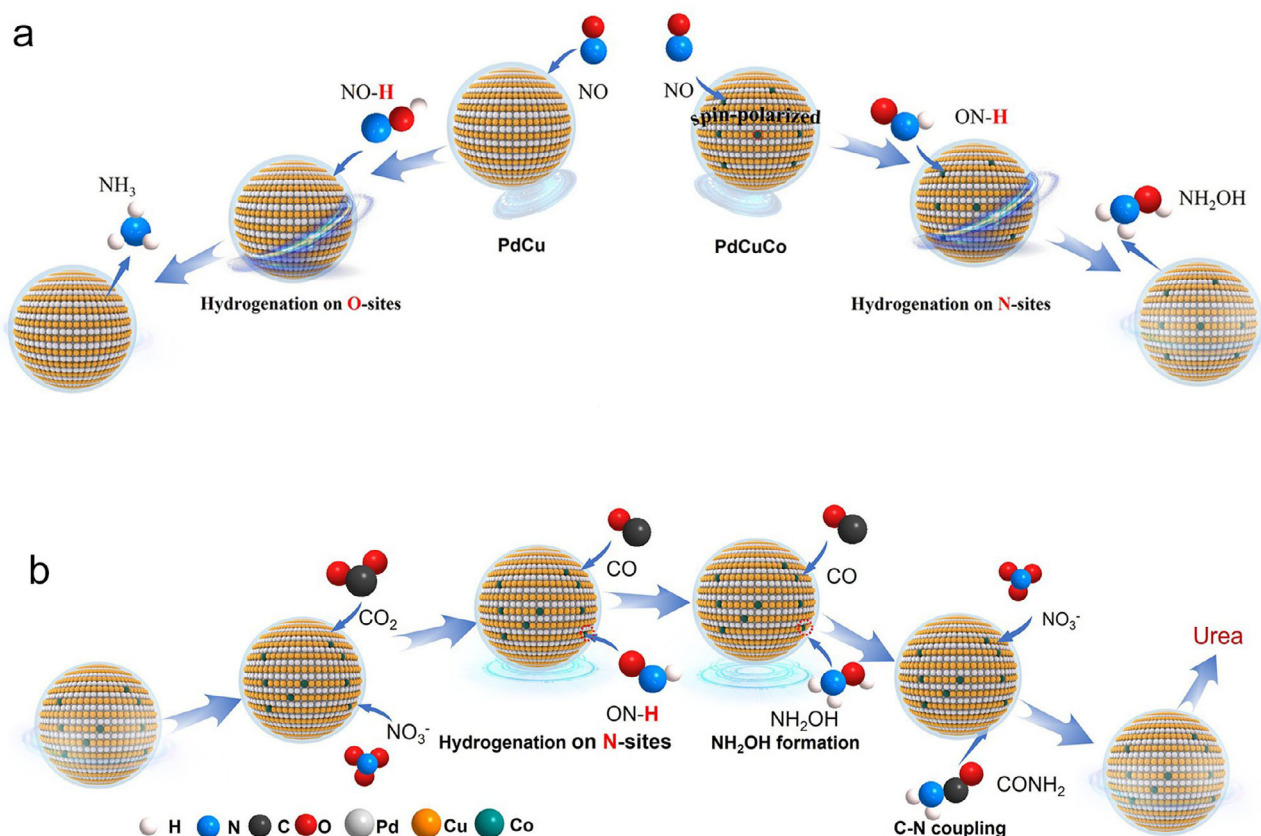


**Figure 1.** a) Schematic illustration of the  $\text{NO}$  hydrogenation position on PdCu and PdCuCo. b) Schematic illustration of the electrocatalytic synthesis of urea from  $\text{NO}_3^-$  and  $\text{CO}_2$  on PdCuCo.

at the N side of  $\text{NO}$  leads to the formation of  $\text{HNO}$  and then hydroxylamine ( $\text{NH}_2\text{OH}$ ), which can further couple with  $\text{CO}$  to form urea.<sup>[10]</sup> On the other hand, the hydrogenation at the O side of  $\text{NO}$  forms  $\text{NOH}$  and subsequently produce  $\text{NH}_3$  as a side product. As  $\text{NO}$  is a spin-polarized molecule, we propose that the catalytic metal sites with spin polarization may allow to tune the binding and hydrogenation position on  $\text{NO}$ , thus capable of switching the subsequent reaction pathways from ammonia to urea. Meanwhile, the as-formed  $\text{NH}_2\text{OH}$  intermediates need to be quickly coupled with carbonic intermediates (e.g.,  $\text{CO}$ ) at the adjacent sites to promote the C–N coupling toward urea.

Inspired by this hypothesis, herein, we developed an atomically ordered, spin-polarized Co-doped PdCu intermetallic compound (designated as PdCuCo), featuring as a highly efficient electrocatalyst for converting  $\text{NO}_3^-$ ,  $\text{CO}_2$ , and water into urea (Figure 1b). The ordered and adjacent Pd and Cu atoms serve as the catalytic sites for adsorption and reduction of  $\text{NO}_3^-$  and  $\text{CO}_2$ , respectively, as well as provide close proximity between the reaction intermediates. More importantly, the introduction of spin-polarized Co atoms can enhance the  $\text{NO}$  binding and hydrogenation on its N side to form  $\text{HNO}$ , which further produces  $\text{NH}_2\text{OH}$ . The subsequent coupling of  $\text{CO}$  and  $\text{NH}_2\text{OH}$  leads to the formation of urea. In contrast, PdCu intermetallic compound without ferromagnetic Co shows a distinctively different selectivity of  $\text{NH}_3$  and  $\text{CO}$ . As a result, the PdCuCo cata-

lyst exhibited an outstanding urea electrocatalytic performance, including a high  $\text{FE}_{\text{urea}}$  of  $81 \pm 4.8\%$ , a urea yield of  $227 \pm 3.0 \text{ mmol} \cdot \text{g}_{\text{cat}}^{-1} \cdot \text{h}^{-1}$ , and an excellent electrochemical stability of  $>260 \text{ h}$ , substantially exceeding most of the previous reports in the electrocatalytic urea synthesis.

## 2. Results and Discussion

### 2.1. Materials Synthesis and Characterization

The PdCuCo intermetallic compound was synthesized via the co-reduction of corresponding metal ions, followed by annealing in  $\text{H}_2/\text{Ar}$  gas to obtain an atomically ordered alloy structure (Methods in the Supporting Information). For comparison, PdCu and PdCuNi intermetallic compounds were also synthesized using a similar approach. The compositions of Pd, Cu, and Co (or Ni) atoms in each sample were quantified using inductively coupled plasma mass spectrometry, from which the measured Pd/Cu/Co ratio in the PdCuCo intermetallic compound was about 50: 45: 5 (Table S1, Supporting Information). The X-ray diffraction (XRD, Figure 2a; Figure S1, Supporting Information) patterns of the PdCuCo, PdCu, and PdCuNi samples all exhibit an ordered, body-centered-cubic (B2) phase (ICSD 181913).<sup>[11]</sup> Transmission electron microscopy (TEM) images of the PdCuCo samples present uniformly dispersed nanoparticles (Figure S2, Supporting Information).

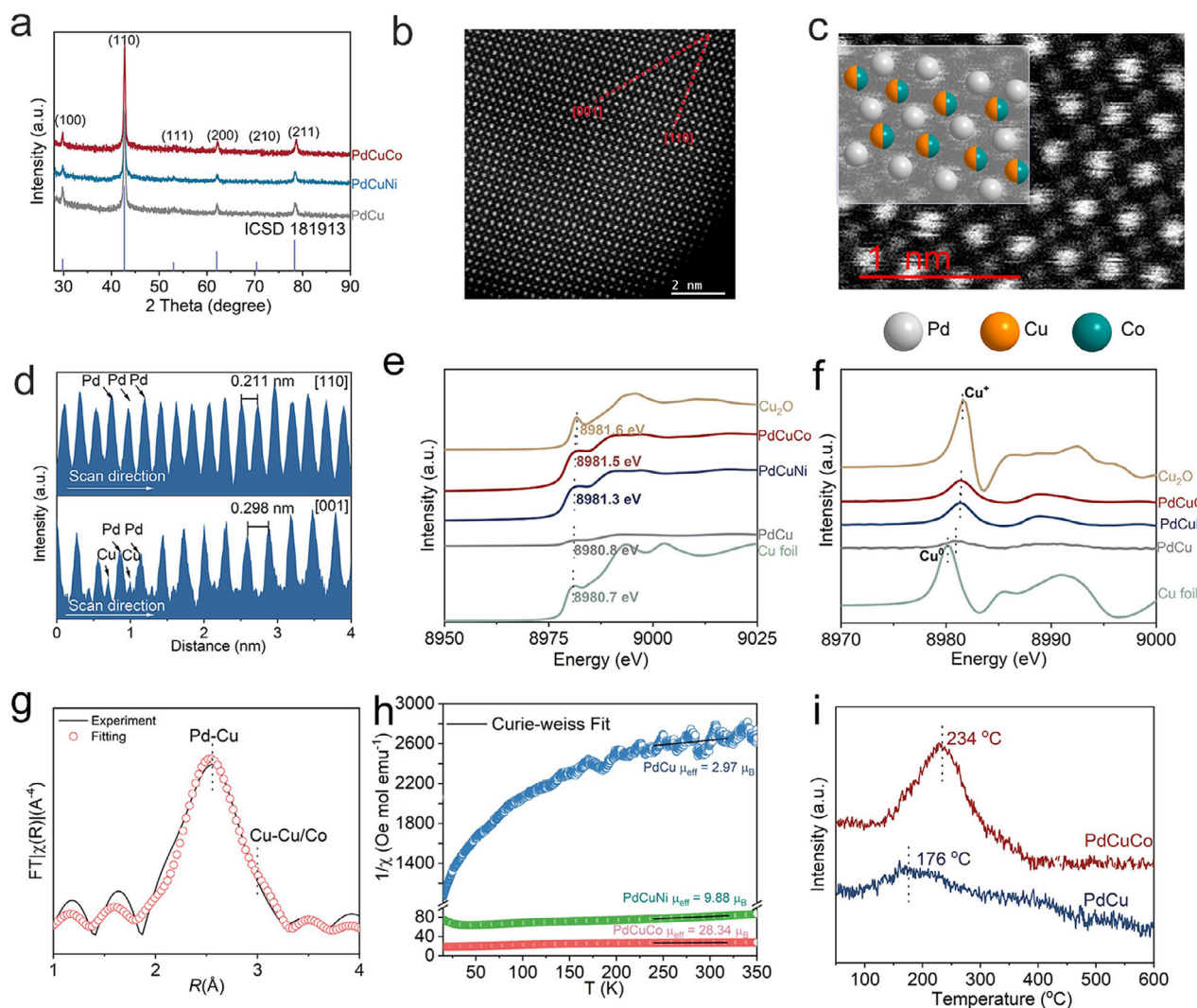


**Figure 2.** Structural characterizations. a) XRD patterns of PdCu, PdCuCo and PdCuNi intermetallic compounds. b) Aberration–corrected HAADF–STEM images of PdCuCo intermetallic compound. c) Enlarged STEM images, where cyan, orange, and grey spheres represent Co, Cu, and Pd atoms, respectively. d) Intensity profiles measured from HAADF–STEM images of PdCuCo intermetallic compound in the [001] and [110] directions, respectively. e) Normalized Cu K–edge XANES spectra and f) first–order derivatives of the XANES spectra of PdCuCo, PdCuNi, and PdCu, in reference with Cu foil and Cu<sub>2</sub>O. g) Experimental Cu K–edge EXAFS spectrum (red circle) and the fitting curve (black curve) of PdCuCo intermetallic compound. h)  $1/\chi_m$  versus temperature plots and the calculated  $\mu_{\text{eff}}$  of PdCuCo, PdCuNi, and PdCu. i) NO temperature–programmed desorption spectra of PdCuCo and PdCu intermetallic compounds.

Energy–dispersive X–ray spectroscopy (EDS) mapping reveals the uniform distributions of Pd, Cu, and Co elements without any phase separation (Figure S3, Supporting Information). The aberration–corrected high–angle annular dark–field scanning transmission electron microscopy (HAADF–STEM) images display highly ordered arrays with alternating bright and dark columns of atoms (Figure 2b,c). The atoms with bright contrast are Pd due to their larger atomic size and mass, and atoms with dark contrast are Cu or Co. The intensity profile transformed from the STEM images presents a periodic oscillation pattern in two directions corresponding to [110] and [001], with the lattice distances of 0.211 and 0.298 nm, respectively (Figure 2d).

X–ray absorption spectroscopy was further conducted to investigate the atomic structures of those samples. The X–ray absorption near–edge structure (XANES) spectra present the Cu absorption edges at 8981.5, 8981.3, and 8980.8 eV for PdCuCo, PdCuNi, and PdCu intermetallic compounds, respectively (Figure 2e,f), which are located between those of Cu and Cu<sub>2</sub>O references, indicating that the partially positive oxidation states of Cu between 0 and 1, in accord with the X–ray photoelectron spectroscopy result (XPS, Figure S4, Supporting Information). The extended X–ray absorption fine structure (EXAFS, Figure 2g; Figure S5, Supporting Information) fittings reveal the bond lengths of Pd–Cu (2.55 Å), Co–Cu (2.97 Å) and Cu–Cu (3.0 Å) in the PdCuCo sample (Table S2, Supporting



Information). The small coordination number of Co–Cu ( $N_{\text{Co–Cu}} = 0.1$ ) suggests the major phase of PdCuCo is similar to the PdCu intermetallic compound.

The magnetization curves of the catalysts were then measured at a magnetic coercivity of 500 Oe at room temperature (Figure S6, Supporting Information). The PdCuCo sample shows a clear ferromagnetic behavior with a smooth hysteresis loop. The saturation value of the total effective magnetic moment on PdCuCo was measured as  $\approx 0.8 \text{ emu g}^{-1}$ , higher than that of PdCuNi ( $\approx 0.2 \text{ emu g}^{-1}$ ) and PdCu ( $\approx 0 \text{ emu g}^{-1}$ ). The temperature-dependent magnetic susceptibility measurement was then conducted to investigate the total effective magnetic moment ( $\mu_{\text{eff}}$ ) of those samples (Figure 2h), which can be determined by the Curie–Weiss law.<sup>[12]</sup> The calculated  $\mu_{\text{eff}}$  values are in the order as: PdCuCo ( $\mu_{\text{eff}} = 28.34 \mu_{\text{B}}$ ) > PdCuNi ( $\mu_{\text{eff}} = 9.88 \mu_{\text{B}}$ ) > PdCu ( $\mu_{\text{eff}} = 2.97 \mu_{\text{B}}$ ), suggesting the existence of the highest unpaired electron spin in PdCuCo.<sup>[13]</sup> In addition, different Co compositions in the PdCuCo samples also result in the increased  $\mu_{\text{eff}}$  values compared to PdCu (Figure S7, Supporting Information), confirming that the Co doping can lead to a higher number of unpaired electrons.

As nitric oxide (NO) is also a critical intermediate formed during the urea electrosynthesis,<sup>[14]</sup> the temperature-programmed desorption (TPD) of NO was then conducted. Compared to PdCu (176 °C), the PdCuCo sample presents a much higher NO desorption temperature (234 °C) and a large peak area (Figure 2i), suggesting the major NO adsorption capacity is contributed by the Co sites.

## 2.2. Electrocatalytic Urea Synthesis

The electrochemical activities of those samples were first conducted in  $\text{KHCO}_3$  electrolyte (without  $\text{NO}_3^-$  and  $\text{CO}_2$ ) to compare the capability of hydrogen evolution reaction (HER, Methods in the Supplementary Information). All the potentials reported in this work were converted in the reversible hydrogen electrode (RHE) scale. The PdCuCo catalyst shows the highest current density among those samples (Figure S8, Supporting Information), indicating the superior HER activity by the introduction of Co sites. The electrocatalytic co-reduction of  $\text{CO}_2$  and  $\text{NO}_3^-$  was then performed (Methods in the Supplementary Information), and the amount of urea product was quantified by two independent spectroscopic methods, i.e., using urease (Figures S9 and S10, Supporting Information)<sup>[5b]</sup> and nuclear magnetic resonance (NMR, Figures S11 and S12, Supporting Information).<sup>[15]</sup> The nitrogen-containing byproducts were determined by UV–Vis spectroscopy (Figure S13, Supporting Information). The electrolyte condition was optimized to perform at 0.1 M  $\text{KHCO}_3$  and  $\text{KNO}_3$  (Figure S14, Supporting Information). The linear sweep voltammetry (LSV) of the PdCuCo electrocatalyst was first conducted in different electrolytes, including  $\text{KHCO}_3$  fed with  $\text{CO}_2$  flow (i.e.,  $\text{CO}_2\text{RR}$  only),  $\text{KNO}_3$  without  $\text{CO}_2$  flow (i.e.,  $\text{NO}_3\text{RR}$  only), and mixed  $\text{KNO}_3$  and  $\text{KHCO}_3$  with  $\text{CO}_2$  flow (i.e., both  $\text{NO}_3\text{RR}$  and  $\text{CO}_2\text{RR}$ ). Under the same applied voltage, the current responses (Figure 3a) are in the order as:  $I_{(\text{NO}_3\text{RR})} > I_{(\text{NO}_3\text{RR}+\text{CO}_2\text{RR})} > I_{(\text{CO}_2\text{RR})}$ , indicating that the co-reduction of  $\text{NO}_3^-$  and  $\text{CO}_2$  can promote  $\text{CO}_2\text{RR}$  while inhibiting  $\text{NO}_3\text{RR}$ , in accord with the previous reports.<sup>[16]</sup> The in situ  $^{13}\text{C}$ -NMR and  $^{15}\text{N}$ -NMR electrolysis using  $^{13}\text{CO}_2$  and  $^{15}\text{NO}_3^-$  reactant iso-

tope labeling verifies the carbon and nitrogen sources in the urea product were from the  $\text{CO}_2$  and  $\text{KNO}_3$  electrolyte, respectively (Figure 3b; Figure S15, Supporting Information). In contrast, the PdCu catalyst exhibits a much weaker NMR signal of urea under same conditions (Figure 3c), suggesting its lower electrocatalytic activity. In addition, the in situ  $^{13}\text{C}$  NMR spectra reveal that the PdCuCo catalyst exhibits a broader full width at half maxima (FWHM) for the  $\text{HCO}_3^-/\text{CO}_3^{2-}$  signals compared to PdCu (Figure 3b,c), suggesting slower exchange dynamics between  $\text{CO}_2$  and  $\text{H}_2\text{O}$  at the interface.<sup>[17]</sup> This slower exchange dynamics favors the  $\text{CO}_2$  retention at the catalytic interface, and enhance the local concentration and residence time of  $^*\text{CO}$  intermediates, thus allowing to facilitate subsequent C–N coupling to urea. Furthermore, the chemical exchange saturation transfer (CEST) spectra provide further evidence supporting this pH variation (Figure S16, Supporting Information), indicating that Co induces water dissociation and generates a higher local concentration of  $\text{H}^+$ . Compared to PdCu with more alkaline local environment, the pH near PdCuCo is close to neutral ( $\approx 7$ ). In addition to urea, other electroreduction products include  $\text{NH}_3$ ,  $\text{CO}$ , formate, and  $\text{H}_2$ , which are not originated from the C–N coupling. The production of urea and  $\text{NH}_3$  shows a competitive trend with respect to the applied potentials. For the PdCuCo catalyst (Figure 3d), urea is the most predominant reduction product in almost the whole potential range tested (between  $-0.3$  and  $-0.9 \text{ V}$ ), with the peak  $j_{\text{urea}}$  of  $11 \pm 1.2 \text{ mA cm}^{-2}$  and  $\text{FE}_{\text{urea}}$  of 81% at  $-0.6 \text{ V}$ . In contrast, for PdCu (Figure 3e), the major reduction product is  $\text{NH}_3$  with the highest  $j_{\text{NH}_3}$  of  $3.0 \pm 0.4 \text{ mA cm}^{-2}$ , while the  $j_{\text{urea}}$  value is  $< 2.0 \text{ mA cm}^{-2}$ . The PdCuNi catalyst shows a urea selectivity between PdCuCo and PdCu, with the peak  $\text{FE}_{\text{urea}}$  of 57% and  $j_{\text{urea}}$  of  $5.0 \text{ mA cm}^{-2}$ , respectively (Figure S17, Supporting Information). The PdCuCo intermetallic compound catalyst exhibit both the highest  $\text{FE}_{\text{urea}}$  values (Figure 3f) and the urea production rates (Figure 3g) among those three samples, with the peak urea production rate of  $227 \pm 3.0 \text{ mmol g}_{\text{cat}}^{-1} \text{ h}^{-1}$  at  $-0.6 \text{ V}$ , substantially exceeding those peak urea yield rates by PdCuNi (i.e.,  $113 \text{ mmol g}_{\text{cat}}^{-1} \text{ h}^{-1}$ , Figure S18, Supporting Information) and PdCu (i.e.,  $24.2 \text{ mmol g}^{-1} \text{ h}^{-1}$ , Figure S19, Supporting Information). Both the electrochemical impedance spectroscopy (EIS, Figure S20, Supporting Information) and cyclic voltammetry measurements (Figure S21, Supporting Information) show that the PdCuCo catalyst presents faster charge transport kinetics and larger electrochemically active surface area (ECSA) compared to those of PdCu and PdCuNi. In addition, the corresponding nitrogen and carbon selectivity in urea (i.e., compared to all the reduction products of  $\text{NO}_3^-$  or  $\text{CO}_2$ ) at  $-0.6 \text{ V}$  reach  $\approx 90\%$  and  $\approx 100\%$ , respectively (Figure 3h), confirming the predominant urea production pathway for both the  $\text{NO}_3^-$  and  $\text{CO}_2$  reactants.

Furthermore, by varying the compositions of different PdCuCo–x samples ( $x = 1\text{--}4$ , Table S1, Supporting Information), the electrocatalytic reduction performances with all product FE values at  $-0.6 \text{ V}$  are displayed (Figure 3i; Figures S22 and S23, Supporting Information). The absence of Cu (e.g., in PdCo) shows the highest  $\text{FE}_{\text{H}_2}$  but negligible selectivities of both urea and  $\text{NH}_3$ , suggesting the critical role of Cu sites for the  $\text{NO}_3^-$  reduction. On the other hand, decreasing the Co content and increasing the Cu content result in the decreased  $\text{FE}_{\text{H}_2}$  and increased  $\text{FE}_{\text{NH}_3}$ , as in PdCu. For the urea production, all the

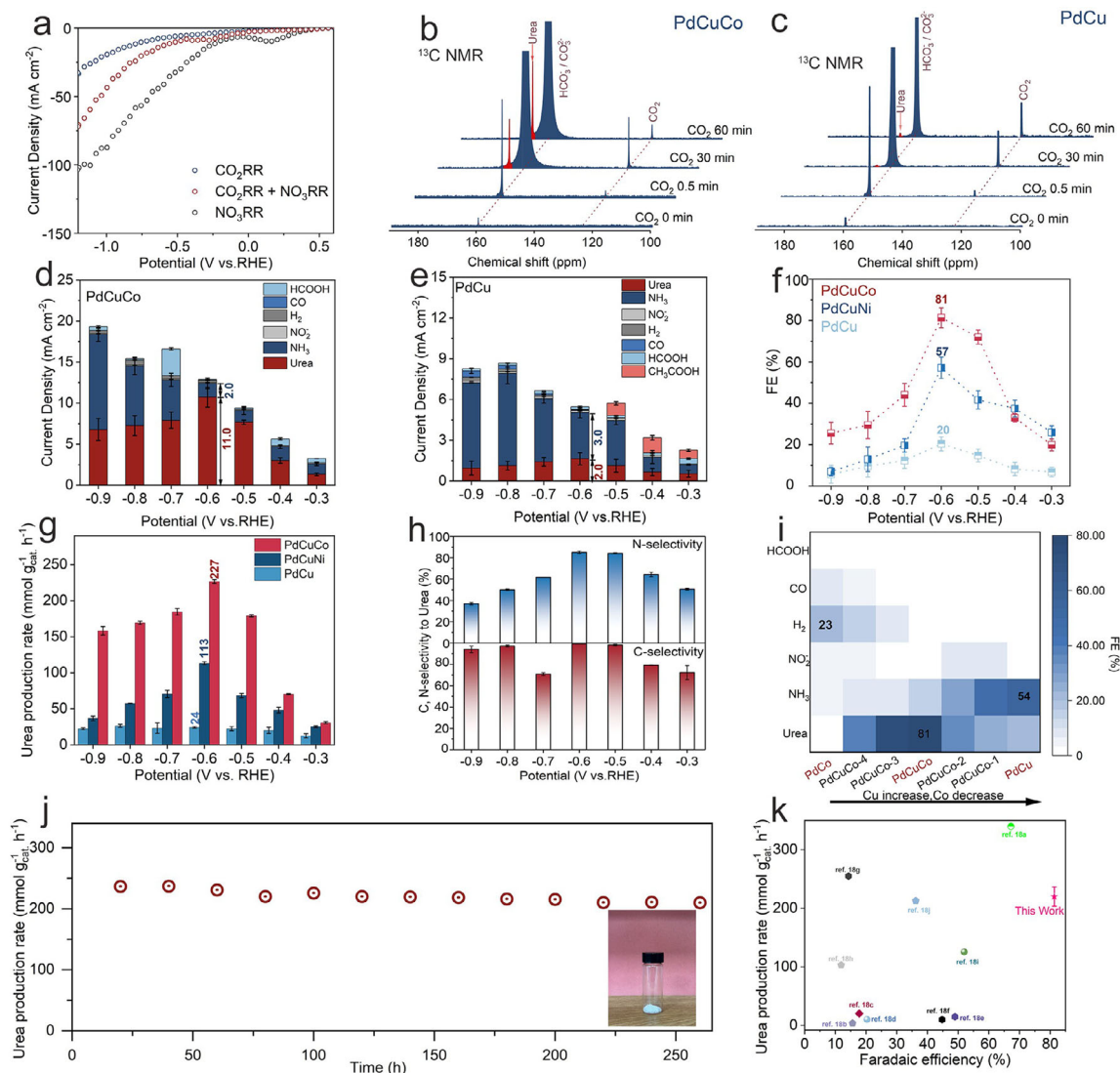


**Figure 3.** C–N coupling electroreduction performance. a) LSV curves of PdCuCo intermetallic compound in  $\text{NO}_3\text{RR}$ ,  $\text{NO}_3\text{RR}+\text{CO}_2\text{RR}$ , and  $\text{CO}_2\text{RR}$ . b,c) In situ  $^{13}\text{C}$ -NMR spectroscopy of (b) PdCuCo and (c) PdCu electrocatalysis under  $^{13}\text{CO}_2$  gas flow. (10 mg of catalyst and 99.9%  $^{13}\text{CO}_2$  in 500.0  $\mu\text{L}$  of  $\text{D}_2\text{O}$ , with electrolyte containing 0.5 M  $\text{KNO}_3$  and 0.5 M  $\text{KHCO}_3$ ). d,e) Partial current densities of the side products of (d) PdCuCo and (e) PdCu. f) Potential-dependent FEs of PdCuCo, PdCuNi, and PdCu intermetallic compounds. g) Potential-dependent urea yield rates of PdCuCo, PdCuNi, and PdCu intermetallic compounds. h) Potential-dependent  $\text{NO}_3^-$ -to-urea (upper panel) and  $\text{CO}_2$ -to-urea (lower panel) selectivities of the PdCuCo intermetallic compound catalyst in urea electrosynthesis. i) Peak FEs of the products of different PdCuCo- $x$  products. j) Cycling stability of the PdCuCo intermetallic compound catalyst for long-time urea electrosynthesis. Inset: photo of the produced urea after purification. k) Comparison of the electrocatalytic urea production performances of PdCuCo intermetallic compound with other representative electrocatalysts reported in the literatures. Error bars corresponded to the mean  $\pm$  standard deviation of  $\geq 3$  measurements.

$\text{FE}_{\text{urea}}$  values of different samples present a volcano-type variation trend with the Co percentage, among which the PdCuCo intermetallic compound catalyst exhibits the highest  $\text{FE}_{\text{urea}}$  (81%) and urea production rate (227  $\text{mmol g}_{\text{cat}}^{-1} \text{h}^{-1}$ ). The PdCuCo catalyst presented a stable urea yield rate of  $220.8 \pm 9.3 \text{ mmol g}_{\text{cat}}^{-1} \text{h}^{-1}$  at  $-0.6 \text{ V}$  versus RHE for 260 h of continuous electrolysis (Figure 3j). After purification, 261.7 mg of urea was obtained from the electrolyte (Figure S24, Supporting Information). The performance of the PdCuCo catalyst outperforms all the previously reported urea electrosynthesis catalysts in both  $\text{FE}_{\text{urea}}$  and urea production rates (Figure 3k).<sup>[18]</sup> After the electrolysis, the

crystal structure, morphology, and elemental composition of the PdCuCo catalyst were well preserved compared with those before electrolysis (Figures S25–S27, Supporting Information), demonstrating its excellent structural stability.

### 2.3. Mechanistic Study

The electrocatalytic urea synthesis mechanism was first tracked by the in situ  $^{19}\text{F}$ -NMR spectroscopy, using a 2-fluorobenzaldehyde (2-FBA) probe to identify

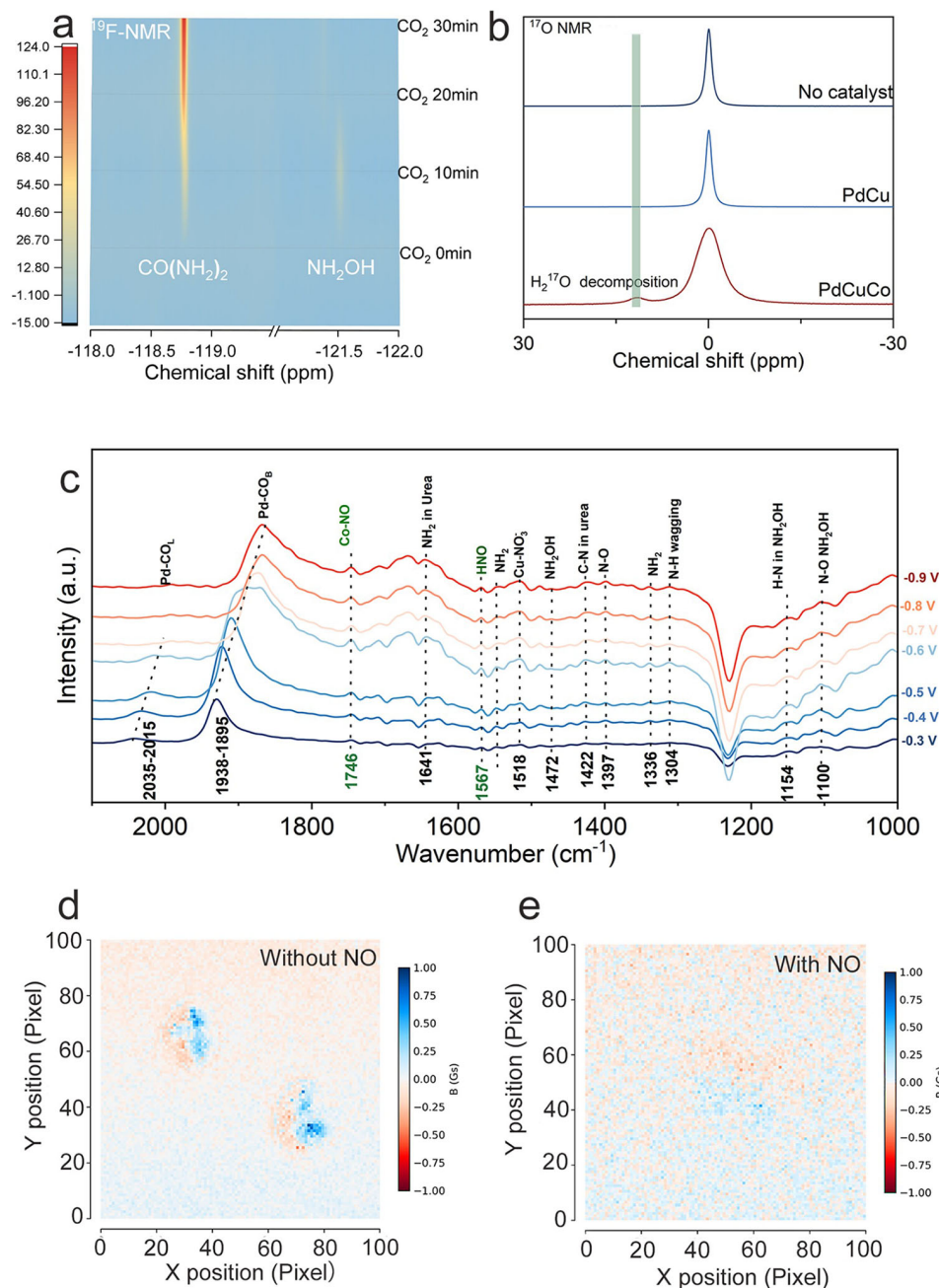


**Figure 4.** a) 2D In situ  $^{19}\text{F}$ -NMR spectra monitoring the production of urea and hydroxylamine of the PdCuCo catalyst by adding 2-FBA probe. b)  $^{17}\text{O}$ -NMR spectroscopy for evaluating the adsorption performance of catalysts to produce  $\text{H}_2^{17}\text{O}$ . (10.0 mg of catalyst in 500.0  $\mu\text{L}$  of  $\text{D}_2\text{O}$  solution containing 0.5 M  $\text{KNO}_3$  and 0.5 M  $\text{KHCO}_3$ , with 10.0  $\mu\text{L}$  of  $\text{H}_2^{17}\text{O}$ ). c) Infrared signals in the range of 1000 to 2100  $\text{cm}^{-1}$ . d,e) Magnetic imaging of the PdCuCo catalyst (d) without NO and (e) with NO.

nitrogen-containing products (Methods in the Supplementary Information). Before the electrolysis, no urea or other nitrogen-containing molecules were observed with the PdCuCo catalyst (Figure 4a). After 10 min of co-electrolysis of  $\text{CO}_2$  and  $\text{NO}_3^-$ , two peaks at -121.47 and -118.81 ppm were observed, corresponding to hydroxylamine ( $\text{NH}_2\text{OH}$ ) and urea ( $\text{CO}(\text{NH}_2)_2$ ), respectively (Figure S28, Supporting Information). The  $\text{NH}_2\text{OH}$  peak was maintained at a similar

intensity during the electrolysis, while the urea peak continued to increase, suggesting that  $\text{NH}_2\text{OH}$  is possibly an intermediate related to the urea formation, in accord with the previous theoretical prediction.<sup>[19]</sup> In addition, the  $^{17}\text{O}$ -NMR spectra indicate that the PdCuCo catalyst presents a much clearer  $^{17}\text{OH}$  peak at a chemical shift of 11.4 ppm than that of PdCu (Figure 4b), suggesting its more efficient water dissociation capability.

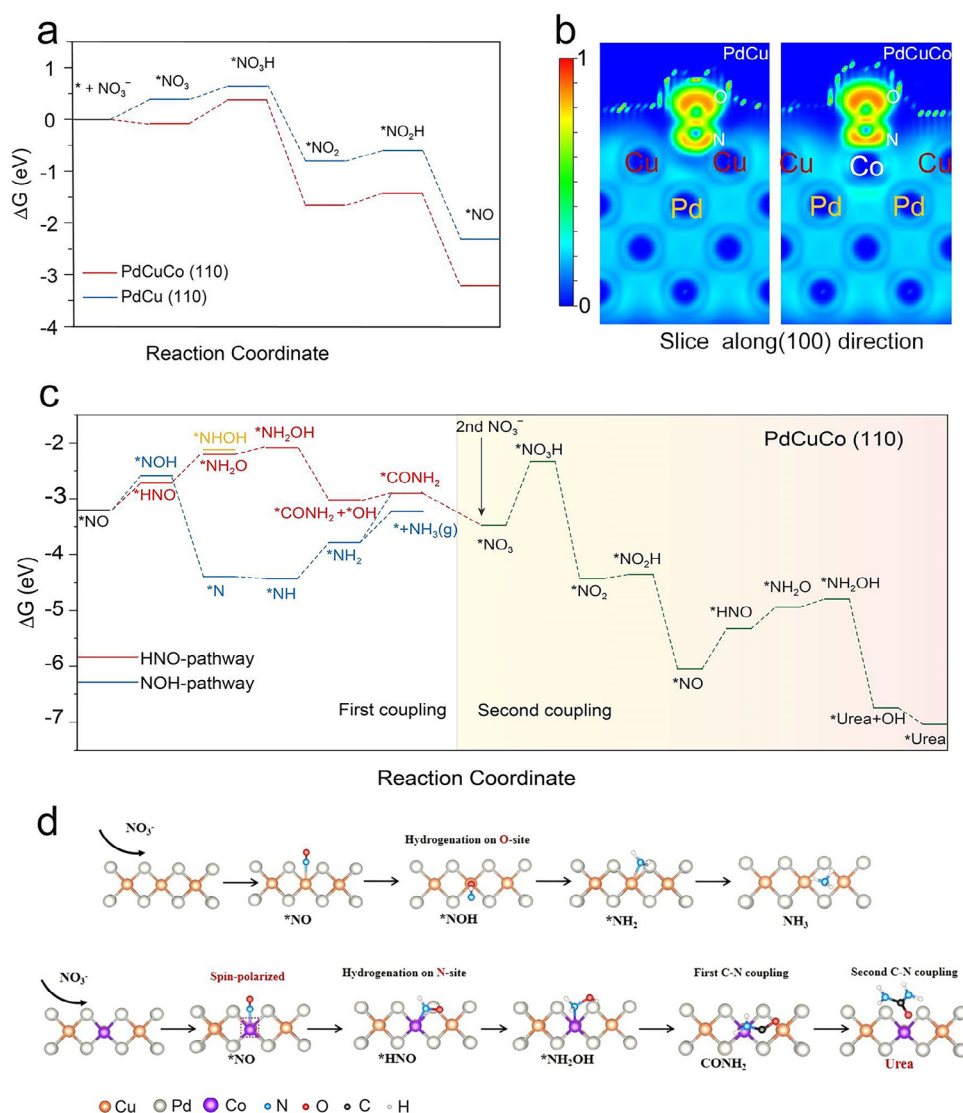


**Figure 5.** a) Energy profiles of each elementary step in  $\text{NO}_3^-$  to  $\text{NO}$  catalyzed by PdCuCo (110) and PdCu (110) planes. b) ELF plots with the most preferred NO adsorption models on PdCu and PdCuCo (110) along [100] direction. c) Energy profiles of each elementary step in C–N coupling. d) Schematic diagram of C–N coupling for urea production in PdCu (110) and PdCuCo (110).

The in situ attenuated total reflection surface-enhanced infrared absorption spectroscopy (ATR–SEIRAS) was then performed to track the evolution of reaction intermediates during the electrocatalytic urea synthesis (Figure 4c; Table S3, Supporting Information). The peaks at 1641 and 1422  $\text{cm}^{-1}$  are ascribed to the  $\text{NH}_2$  characteristic peak and C–N bond of urea.<sup>[4,20]</sup> The peaks at 1100, 1154, and 1472  $\text{cm}^{-1}$  are attributed to  $\text{NH}_2\text{OH}$ ,<sup>[20,21]</sup> confirming that the existence of  $\text{*NH}_2\text{OH}$  intermediate during the urea formation pathway. In addition, the two bands at 1938–1895 and 2035–2015  $\text{cm}^{-1}$  are assigned to the CO bridged adsorption and atop adsorption on Pd atoms (i.e., Pd–CO<sub>B</sub> and Pd–CO<sub>L</sub>), respectively,<sup>[22]</sup> and the 1518  $\text{cm}^{-1}$  peak is ascribed to  $\text{NO}_3^-$  adsorbed on Cu (i.e., Cu–NO<sub>3</sub><sup>−</sup>),<sup>[23]</sup> indicating the electroreduction of CO<sub>2</sub> and NO<sub>3</sub><sup>−</sup> take place at the Pd and Cu sites, respectively. For PdCuCo, the peak at 1746  $\text{cm}^{-1}$  is attributed to the adsorption of NO on Co atoms,<sup>[24]</sup> which

is not observed in PdCu (Figure S29, Supporting Information), suggesting that the NO molecules in situ generated from NO<sub>3</sub><sup>−</sup> tend to adsorb on the Co sites. The peak at 1567  $\text{cm}^{-1}$  is attributed to the adsorption peak of HNO,<sup>[24c]</sup> confirming that the hydrogenation position of  $\text{*NO}$  is on the N side.

The binding of NO intermediate on the Co sites was then investigated via magnetic imaging of the PdCuCo catalyst in the presence or absence of NO molecules, respectively, using nitrogen–vacancy (NV) centers in diamond as quantum sensors (Methods in the Supplementary Information).<sup>[25]</sup> For PdCu (Figure S30, Supporting Information), the NV–based magnetic imaging did not present any observable signal, either with or without the presence of NO. In contrast, the PdCuCo catalyst showed strong magnetic imaging signal before the NO treatment (Figure 4d), while the signal was substantially reduced when the sample was pre-incubated in a NO-containing atmosphere



(Figure 4e), confirming that NO molecules are bound on the spin-polarized Co sites.<sup>[9]</sup> This experiment is consistent with our calculation of the spin density on different samples, among which the PdCuCo sample shows the highest spin polarization value of  $2.736 \mu_B$  (Figure S31, Supporting Information). Together, our experiments indicate that the Co site with unpaired electrons in PdCuCo can generate strong spin polarization, and also serve as the binding sites for NO.

## 2.4. Theoretical Calculations

Density functional theory (DFT) calculations were conducted to investigate the reaction mechanisms on the Co-doping into PdCu intermetallic compound with different selectivities (Methods in the Supplementary Information). The PdCu (110) surface was used for the calculations according to our XRD data (Figures S32 and S33, Supporting Information). First, the free energy changes of  $\text{NO}_3^-$  reduction to NO were calculated for both PdCuCo and PdCu, respectively (Figure 5a). PdCuCo presents a more exothermic process than that of on PdCu (i.e.,  $-3.2$  vs.  $-2.3$  eV), suggesting the enhancement of  $^*\text{NO}$  adsorption on PdCuCo. Second, the most preferable adsorption position of  $^*\text{NO}$  on PdCu (110) is calculated as the bridged site between Pd and Cu (Figure S34, Supporting Information), while on PdCuCo (110), the most preferable position shifts to the Co atom (Figure S35, Supporting Information), in accord with the aforementioned experimental result that Co is the adsorption site for  $^*\text{NO}$ . In addition, Pd is calculated as the adsorption site for  $^*\text{CO}$  (Figure S36, Supporting Information), consistent with our ATR-SEIRAS observation. Third, the electron localization function (ELF) image analysis further reveals that the  $^*\text{NO}$  molecule adsorbed on PdCuCo presents an increased localized electron density on its N-terminal than that adsorbed on PdCu (Figure 5b), suggesting the enhanced hydrogenation capability on the N-terminal of  $^*\text{NO}$ .

The reaction pathways of  $\text{CO}_2$  and  $^*\text{NO}$  to urea were further calculated. For PdCuCo (110) (Figure 5c; Figure S37, Supporting Information), the hydrogenation energy on the N-terminal of  $^*\text{NO}$  (to form  $^*\text{HNO}$ ) is  $0.06$  eV lower than that on the O-terminal (to form  $^*\text{NOH}$ ). The  $^*\text{HNO}$  intermediate is further converted into  $^*\text{NH}_2\text{OH}$  on the Co site, followed by coupling with CO to form  $^*\text{CONH}_2$  and shifting to the Pd site. Afterward, the second  $\text{NO}_3^-$  is adsorbed onto the open Co site and reduced to  $\text{NH}_2\text{OH}$ , allowing for the second C–N coupling to produce urea. The top and side views of the most stable adsorption configurations on the PdCuCo surface are displayed (Figures S38 and S39, Supporting Information). In contrast, for PdCu (110) (Figures S40 and S41, Supporting Information), the hydrogenation of  $^*\text{NO}$  tends to take place on the O-terminal to form  $^*\text{NOH}$ , which leads to the preferential formation of  $^*\text{NH}_2$ , instead of  $^*\text{NH}_2\text{OH}$ . The subsequent hydrogenation of  $^*\text{NH}_2$  to  $\text{NH}_3$  is much more energy preferable than its C–N coupling with CO (i.e.,  $-0.71$  vs.  $0.64$  eV), thus resulting in the main product as  $\text{NH}_3$ , in good accord with our experimental observation.

Based on the aforementioned results, the urea electrosynthesis mechanism are proposed. For the PdCuCo intermetallic compound (Figure 5d), the introduction of spin-polarized Co atom enhances the reduction of  $\text{NO}_3^-$  to NO, as well as the adsorption of the  $^*\text{NO}$  intermediate on the Co site. The subsequent hydro-

genation of  $^*\text{NO}$  takes place at the N-terminal to form  $^*\text{HNO}$  intermediate, which leads to the production of  $^*\text{NH}_2\text{OH}$  and eventually urea. On the other hand, the binding of  $^*\text{NO}$  on the PdCu intermetallic compound is at the O-terminal, resulting in the generation of  $^*\text{NOH}$  and finally forming  $\text{NH}_3$ .

## 3. Conclusion

In summary, we have developed a spin-polarized electrocatalyst by doping ferromagnetic Co atoms into PdCu intermetallic compound. The atomically ordered intermetallic compound allows efficient adsorption and subsequent C–N coupling of reactive intermediates. The presence of Co atoms enhances the binding of  $^*\text{NO}$  intermediate, tunes the position of hydrogenation at the N-terminal, and subsequently forms  $^*\text{NH}_2\text{OH}$  intermediate toward the urea electrosynthesis pathway. In contrast, the PdCu without spin polarization shows the hydrogenation of  $^*\text{NO}$  at the O-terminal, with the final product as ammonia. The PdCuCo intermetallic compound catalyst exhibited an outstanding performance for the electrochemical conversion of  $\text{NO}_3^-$  and  $\text{CO}_2$  into urea, including a high urea production rate of  $227 \text{ mmol g}_{\text{cat}}^{-1} \text{ h}^{-1}$ ,  $\text{FE}_{\text{urea}}$  of 81%, and a long electrolysis stability of  $>260$  h. Our work suggests an attractive feature of developing spin-polarized intermetallic compounds for efficient electrocatalysts for C–N coupling toward different value-added products.

## Supporting Information

Supporting Information is available from the Wiley Online Library or from the author.

## Acknowledgements

M.X. and H.Z. contributed equally to this work. The authors thank the following grants for supporting this work: the National Key Research and Development Program of China (2024YFB4106400, 2024YFB4106401), the National Natural Science Foundation of China (22025502, U23A20552, 22072045, 22222901, 22175022). Prof. Qing Han was further supported by the “Xiaomi” Young Investigator Award. The authors thank the BL11B in the Shanghai Synchrotron Radiation Facility for the XAFS measurement. The computations in this research were performed using the CFFF platform of Fudan University.

## Conflict of Interest

The authors declare no conflict of interest.

## Data Availability Statement

The data that support the findings of this study are available from the corresponding author upon reasonable request.

## Keywords

carbon–nitrogen coupling, hydroxylamine, intermetallic compound, spin-polarized, urea

Received: March 18, 2025

Revised: April 7, 2025

Published online:



- [1] Z. Zhang, D. Li, Y. Tu, J. Deng, H. Bi, Y. Yao, Y. Wang, T. Li, Y. Luo, S. Sun, D. Zheng, S. A. C. Carabineiro, Z. Chen, J. Zhu, X. Sun, *SusMat*. **2024**, 4, 193.
- [2] X. Fan, C. Liu, X. He, Z. Li, L. Yue, W. Zhao, J. Li, Y. Wang, T. Li, Y. Luo, D. Zheng, S. Sun, Q. Liu, L. Li, W. Chu, F. Gong, B. Tang, Y. Yao, X. Sun, *Adv. Mater.* **2024**, 36, 2401221.
- [3] J. Chen, L. Wang, *Adv. Mater.* **2022**, 34, 2103900.
- [4] C. Lv, L. Zhong, H. Liu, Z. Fang, C. Yan, M. Chen, Y. Kong, C. Lee, D. Liu, S. Li, J. Liu, L. Song, G. Chen, Q. Yan, G. Yu, *Nat. Sustain.* **2021**, 4, 868.
- [5] a) Y. Luo, K. Xie, P. Ou, C. Lavallais, T. Peng, Z. Chen, Z. Zhang, N. Wang, X.-Y. Li, I. Grigioni, B. Liu, D. Sinton, J. B. Dunn, E. H. Sargent, *Nat. Catal.* **2023**, 6, 939; b) M. Xu, F. Wu, Y. Zhang, Y. Yao, G. Zhu, X. Li, L. Chen, G. Jia, X. Wu, Y. Huang, P. Gao, W. Ye, *Nat. Commun.* **2023**, 14, 6994.
- [6] Y. Zhao, Y. Ding, W. Li, C. Liu, Y. Li, Z. Zhao, Y. Shan, F. Li, L. Sun, F. Li, *Nat. Commun.* **2023**, 14, 4491.
- [7] X. Chen, S. Lv, J. Kang, Z. Wang, T. Guo, Y. Wang, G. Teobaldi, L. M. Liu, L. Guo, *Proc. Natl Acad. Sci. USA* **2023**, 120, 2306841120.
- [8] Z. Huang, B. Yang, Y. Zhou, W. Luo, G. Chen, M. Liu, X. Liu, R. Ma, N. Zhang, *ACS Nano* **2023**, 17, 25091.
- [9] P. Guo, D. Luan, H. Li, L. Li, S. Yang, J. Xiao, *J. Am. Chem. Soc.* **2024**, 146, 13974.
- [10] a) S.-K. Geng, Y. Zheng, S.-Q. Li, H. Su, X. Zhao, J. Hu, H.-B. Shu, M. Jaroniec, P. Chen, Q.-H. Liu, S.-Z. Qiao, *Nat. Energy* **2021**, 6, 904; b) L. Wu, J. Feng, L. Zhang, S. Jia, X. Song, Q. Zhu, X. Kang, X. Xing, X. Sun, B. Han, *Angew. Chem., Int. Ed.* **2023**, 62, 202307952.
- [11] Y. Ji, Z. Chen, R. Wei, C. Yang, Y. Wang, J. Xu, H. Zhang, A. Guan, J. Chen, T.-K. Sham, J. Luo, Y. Yang, X. Xu, G. Zheng, *Nat. Catal.* **2022**, 5, 251.
- [12] J. Dai, Y. Tong, L. Zhao, Z. Hu, C.-T. Chen, C.-Y. Kuo, G. Zhan, J. Wang, X. Zou, Q. Zheng, W. Hou, R. Wang, K. Wang, R. Zhao, X.-K. Gu, Y. Yao, L. Zhang, *Nat. Commun.* **2024**, 15, 88.
- [13] Y.-N. Gong, W. Zhong, Y. Li, Y. Qiu, L. Zheng, J. Jiang, H.-L. Jiang, *J. Am. Chem. Soc.* **2020**, 142, 16723.
- [14] L. Chen, C. Tang, Y. Zheng, K. Davey, Y. Jiao, *Sci. China Mater.* **2023**, 66, 2346.
- [15] X. Wei, X. Wen, Y. Liu, C. Chen, C. Xie, D. Wang, M. Qiu, N. He, P. Zhou, W. Chen, J. Cheng, H. Lin, J. Jia, X. Z. Fu, S. Wang, *J. Am. Chem. Soc.* **2022**, 144, 11530.
- [16] a) D. Wang, C. Chen, S. Wang, *Sci. China Chem.* **2022**, 66, 1052; b) Q. Hu, W. Zhou, S. Qi, Q. Huo, X. Li, M. Lv, X. Chen, C. Feng, J. Yu, X. Chai, H. Yang, C. He, *Nat. Sustain.* **2024**, 7, 442.
- [17] a) B. B. Xu, Y. Liu, Y. Liu, X. You, H. Zhou, Y. N. Xu, P. F. Liu, H. F. Wang, H. G. Yang, X. L. Wang, Y. F. Yao, *Chem* **2024**, 10, 3114; b) X.-M. You, B. Xu, H. Zhou, H. Qiao, X. Lv, Z. Huang, J. Pang, L. Yang, P. F. Liu, X. Guan, H. G. Yang, X. Wang, Y.-F. Yao, *ACS Nano* **2024**, 18, 9403.
- [18] a) D.-S. Huang, X.-F. Qiu, J.-R. Huang, M. Mao, L. Liu, Y. Han, Z.-H. Zhao, P.-Q. Liao, X.-M. Chen, *Nat. Synth.* **2024**, 3, 1404; b) H. Wang, Y. Jiang, S. Li, F. Gou, X. Liu, Y. Jiang, W. Luo, W. Shen, R. He, M. Li, *Appl. Catal. B* **2022**, 318, 121819; c) X. Zhang, X. Zhu, S. Bo, C. Chen, M. Qiu, X. Wei, N. He, C. Xie, W. Chen, J. Zheng, P. Chen, S. P. Jiang, Y. Li, Q. Liu, S. Wang, *Nat. Commun.* **2022**, 13, 5337; d) Y. Mao, Y. Jiang, Q. Gou, S. Lv, Z. Song, Y. Jiang, W. Wang, M. Li, L. Zheng, W. Su, R. He, *Appl. Catal. B* **2024**, 340, 123189; e) M. Yuan, J. Chen, H. Zhang, Q. Li, L. Zhou, C. Yang, R. Liu, Z. Liu, S. Zhang, G. Zhang, *Energy Environ. Sci.* **2022**, 15, 2084; f) Y. Zhang, X. Fan, X. He, T. Yan, Y. Yao, D. Zheng, J. Zhao, Q. Cai, Q. Liu, L. Li, W. Chu, S. Sun, X. Sun, *Chin. Chem. Lett.* **2024**, 35, 109806; g) Y. Wang, X. Zhu, Q. An, X. Zhang, X. Wei, C. Chen, H. Li, D. Chen, Y. Zhou, Q. Liu, H. Shao, S. Wang, *Angew. Chem., Int. Ed.* **2024**, 63, 202410938; h) H. Li, L. Xu, S. Bo, Y. Wang, H. Xu, C. Chen, R. Miao, D. Chen, K. Zhang, Q. Liu, J. Shen, H. Shao, J. Jia, S. Wang, *Nat. Commun.* **2024**, 15, 8858; i) S. Shin, S. Sultan, Z.-X. Chen, H. Lee, H. Choi, T.-U. Wi, C. Park, T. Kim, C. Lee, J. Jeong, H. Shin, T.-H. Kim, H. Ju, H. C. Yoon, H.-K. Song, H.-W. Lee, M.-J. Cheng, Y. Kwon, *Energy Environ. Sci.* **2023**, 16, 2003; j) X. Tu, X. Zhu, S. Bo, X. Zhang, R. Miao, G. Wen, C. Chen, J. Li, Y. Zhou, Q. Liu, D. Chen, H. Shao, D. Yan, Y. Li, J. Jia, S. Wang, *Angew. Chem., Int. Ed.* **2024**, 63, 202317087.
- [19] C. S. Gerke, Y. Xu, Y. Yang, G. D. Foley, B. Zhang, E. Shi, N. M. Bedford, F. Che, V. S. Thoi, *J. Am. Chem. Soc.* **2023**, 145, 26144.
- [20] R. K. O. D. R. V. Alsenoy, *J. Phys. Chem. A* **1999**, 103, 4621.
- [21] a) J.-Y. Fang, Q.-Z. Zheng, Y.-Y. Lou, K.-M. Zhao, S.-N. Hu, G. Li, O. Akdim, X.-Y. Huang, S.-G. Sun, *Nat. Commun.* **2022**, 13, 7899; b) J. Wu, L. Xu, Z. Kong, K. Gu, Y. Lu, X. Wu, Y. Zou, S. Wang, *Angew. Chem., Int. Ed.* **2023**, 62, 202311196.
- [22] a) T.-W. Jiang, Y.-W. Zhou, X.-Y. Ma, X. Qin, H. Li, C. Ding, B. Jiang, K. Jiang, W.-B. Cai, *ACS Catal.* **2021**, 11, 840; b) D. Gao, H. Zhou, F. Cai, D. Wang, Y. Hu, B. Jiang, W.-B. Cai, X. Chen, R. Si, F. Yang, S. Miao, J. Wang, G. Wang, X. Bao, *Nano Res.* **2017**, 10, 2181; c) R. De, S. Gonglach, S. Paul, M. Haas, S. S. Sreejith, P. Gerschel, U. P. Apfel, T. H. Vuong, J. Rabeah, S. Roy, W. Schofberger, *Angew. Chem., Int. Ed.* **2020**, 59, 10527.
- [23] J. Sun, H. Yang, W. Gao, T. Cao, G. Zhao, *Angew. Chem., Int. Ed.* **2022**, 61, 202211373.
- [24] a) C. De La Cruz, N. Sheppard, *Spectrochim. Acta Part A* **2011**, 78, 7; b) J. Zhou, S. Han, R. Yang, T. Li, W. Li, Y. Wang, Y. Yu, B. Zhang, *Angew. Chem., Int. Ed.* **2023**, 62, 202305184.
- [25] T. Staudacher, F. Shi, S. Pezzagna, J. Meijer, J. Du, C. A. Meriles, F. Reinhard, J. Wrachtrup, *Science* **2013**, 339, 561.